

Retrieving stellar parameters and dynamics of AGB stars with *Gaia* parallax measurements and CO⁵BOLD RHD simulations

E. Béguin¹, A. Chiavassa¹, A. Ahmad², B. Freytag², and S. Uttenthaler³

¹ Université Côte d’Azur, Observatoire de la Côte d’Azur, CNRS, Lagrange, CS 34229, Nice, France
e-mail: e.lysabeth.beguin@oca.eu

² Theoretical Astrophysics, Department of Physics and Astronomy, Uppsala University, Box 516, SE-751 20 Uppsala, Sweden

³ Institute of Applied Physics, TU Wien, Wiedner Hauptstraße 8-10, 1040 Vienna, Austria

Received April 4, 2024; accepted July 16, 2024

ABSTRACT

Context. The complex dynamics of asymptotic giant branch (AGB) stars and the resulting stellar winds have a significant impact on the measurements of stellar parameters and amplify their uncertainties. Three-dimensional (3D) radiative hydrodynamic (RHD) simulations of convection suggest that convection-related structures at the surface of AGB star affect the photocentre displacement and the parallax uncertainty measured by *Gaia*.

Aims. We explore the impact of the convection on the photocentre variability and aim to establish analytical laws between the photocentre displacement and stellar parameters to retrieve such parameters from the parallax uncertainty.

Methods. We used a selection of 31 RHD simulations with CO⁵BOLD and the post-processing radiative transfer code OPTIM3D to compute intensity maps in the *Gaia* G band [320–1050 nm]. From these maps, we calculated the photocentre position and temporal fluctuations. We then compared the synthetic standard deviation to the parallax uncertainty of a sample of 53 Mira stars observed with *Gaia*.

Results. The simulations show a displacement of the photocentre across the surface ranging from 4 to 13% of the corresponding stellar radius, in agreement with previous studies. We provide an analytical law relating the pulsation period of the simulations and the photocentre displacement as well as the pulsation period and stellar parameters. By combining these laws, we retrieve the surface gravity, the effective temperature, and the radius for the stars in our sample.

Conclusions. Our analysis highlights an original procedure to retrieve stellar parameters by using both state-of-the-art 3D numerical simulations of AGB stellar convection and parallax observations of AGB stars. This will help us refine our understanding of these giants.

Key words. Stars: Atmospheres – Stars: AGB and post-AGB – Astrometry – Parallaxes – Hydrodynamics

1. Introduction

Low- to intermediate-mass stars ($0.8 - 8 M_{\odot}$) evolve into the asymptotic giant branch (AGB), in which they undergo complex dynamics characterised by several processes including convection, pulsations, and shockwaves. These processes trigger strong stellar winds ($10^{-8} - 10^{-5} M_{\odot}/\text{yr}$, De Beck et al. 2010) that significantly enrich the interstellar medium with various chemical elements (Höfner & Olofsson 2018). These processes and stellar winds also amplify uncertainties of stellar parameter determinations with spectro-photometric techniques, like the effective temperature, which in turn impacts the determination of mass-loss rates (Höfner & Olofsson 2018). In particular, Mira stars are peculiar AGB stars, showing extreme magnitude variability (larger than 2.5 mag in the visible) due to pulsations over periods of 100 to 1000 days (Decin 2021).

In Chiavassa et al. (2011, 2018, 2022), 3D radiative hydrodynamics (RHD) simulations of convection computed with CO⁵BOLD (Freytag et al. 2012; Freytag 2013, 2017) reveal the AGB photosphere morphology to be made of a few large-scale, long-lived convective cells and some short-lived and small-scale structures that cause temporal fluctuations on the emerging intensity in the *Gaia* G band [320–1050 nm]. The authors suggest that the temporal convective-related photocentre variability should substantially impact the photometric measurements

of *Gaia*, and thus the parallax uncertainty. In this work, we use 31 recent simulations to establish analytical laws between the photocentre displacement and the pulsation period and then between the pulsation period and stellar parameters. We combine these laws and apply them to a sample of 53 Mira stars from Uttenthaler et al. (2019) to retrieve their effective stellar gravity, effective temperature, and radius thanks to their parallax uncertainty from *Gaia* Data Release 3¹ (GDR3) (Gaia Collaboration et al. 2016, 2023).

2. Overview of the radiative hydrodynamics simulations

In this section, we present the simulations and the theoretical relations between the stellar parameters and the pulsation period. We also present how we compute the standard deviation of the photocentre displacement and its correlation with the pulsation period.

¹ GDR3 website: <https://www.cosmos.esa.int/web/gaia/data-release-3>

2.1. Methods

We used RHD simulations of AGB stars computed with the code CO⁵BOLD (Freytag et al. 2012; Freytag 2013, 2017). It solves the coupled non-linear equations of compressible hydrodynamics and non-local radiative energy transfer, assuming solar abundances, which is appropriate for M-type AGB stars. The configuration is ‘star-in-a-box’, which takes into account the dynamics of the outer convective envelope and the inner atmosphere. Convection and pulsations in the stellar interior trigger shocks in the outer atmosphere, giving a direct insight into the stellar stratification. Material can levitate towards layers where it can condensate into dust grains (Freytag & Höfner 2023). However, models used in this work do not include dust.

We then post-processed a set of temporal snapshots from the RHD simulations using the radiative transfer code OPTIM3D (Chiavassa et al. 2009), which takes into account the Doppler shifts, partly due to convection, in order to compute intensity maps integrated over the *Gaia* G band [320–1050 nm]. The radiative transfer is computed using pre-tabulated extinction coefficients from MARCS models (Gustafsson et al. 2008) and solar abundance tables (Asplund et al. 2009).

2.2. Characterising the AGB stellar grid

We used a selection of simulations from Freytag et al. (2017), Chiavassa et al. (2018) [abbreviation: F17+C18], Ahmad et al. (2023) [abbreviation: A23] and some new models [abbreviation: This work], in order to cover the 2000–10000 L_⊙ range. The updated simulation parameters are reported in Table A.1.

In particular, 24 simulations have a stellar mass equal to 1.0 M_⊙, and seven simulations have one equal to 1.5 M_⊙. In the rest of this work, we denote by a 1.0 subscript the laws or the results obtained from the analysis of the 1.0 M_⊙ simulations; and by a 1.5 subscript those obtained from the analysis of the 1.5 M_⊙ simulations.

The pressure scale height is defined as $H_p = \frac{k_B T_{\text{eff}}}{\mu g}$, with k_B the Boltzmann constant, T_{eff} the effective surface temperature, μ the mean molecular mass, and g the local surface gravity. The lower the surface gravity is, the larger the pressure scale height becomes, and so the larger the convective cells can grow (see Fig. 1 and Freytag et al. (2017)).

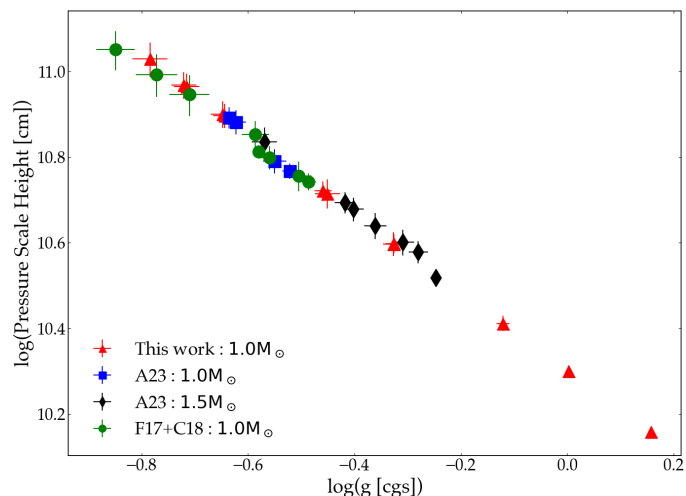


Fig. 1. Log-log plot of the surface gravity [cgs] versus the pressure scale height [cm]. As the effective temperature is near constant among all our models, we expect a linear relation.

Moreover, Freytag et al. (1997) estimated that the characteristic granule size scales linearly with H_p . Interplay between large-scale convection and radial pulsations results in the formation of giant and bright convective cells at the surface. The resulting intensity asymmetries directly cause temporal and spatial fluctuations of the photocentre. The larger the cells, the larger the photocentre displacement. This results in a linear relation between the photocentre displacement and the pressure scale height (Chiavassa et al. 2011, 2018). However, Chiavassa et al. (2011) found it is no longer true for H_p greater than 2.24×10^{10} cm for both interferometric observations of red supergiant stars and 3D simulations, suggesting that the relation for evolved stars is more complex and depends on H_p (Fig. 18 in the aforementioned article).

Concerning the pulsation period, Ahmad et al. (2023) performed a fast Fourier transform on spherically averaged mass flows of the CO⁵BOLD snapshots to derive the radial pulsation periods. The derived bolometric luminosity–period relation suggests good agreement between the pulsation periods obtained from the RHD simulations and from available observations. They are reported in columns 9 and 10 in Table A.1.

Ahmad et al. (2023) found a correlation between the pulsation period and the surface gravity ($g \propto M_\star/R_\star^2$, see Eq. (4) in the aforementioned article). Thus, the pulsation period increases when the surface gravity decreases. In agreement with this study, we found a linear relation between $\log(P_{\text{puls}})$ and $\log(g)$, see Fig. 2. By minimising the sum of the squares of the residuals between the data and a linear function as in the non-linear least-squares problem, we computed the most suitable parameters of the linear law. We also computed the reduced $\bar{\chi}^2$ for the 1.0 M_⊙ simulations and for the 1.5 M_⊙ simulations: $\bar{\chi}_{1.0}^2 = 2.2$ and $\bar{\chi}_{1.5}^2 = 0.4$. The linear law found in each case is expressed as follows:

$$\log(P_{\text{puls}}) = -0.84 \cdot \log(g) + 2.14, \quad \text{for } M_\star = 1.0 M_\odot \quad (1)$$

$$\log(P_{\text{puls}}) = -0.78 \cdot \log(g) + 2.20, \quad \text{for } M_\star = 1.5 M_\odot. \quad (2)$$

It is important to note that the $\bar{\chi}_{1.5}^2$ value is lower than $\bar{\chi}_{1.0}^2$ because there are only seven points to fit (i.e. seven RHD simulations at 1.5 M_⊙) and they are less scattered.

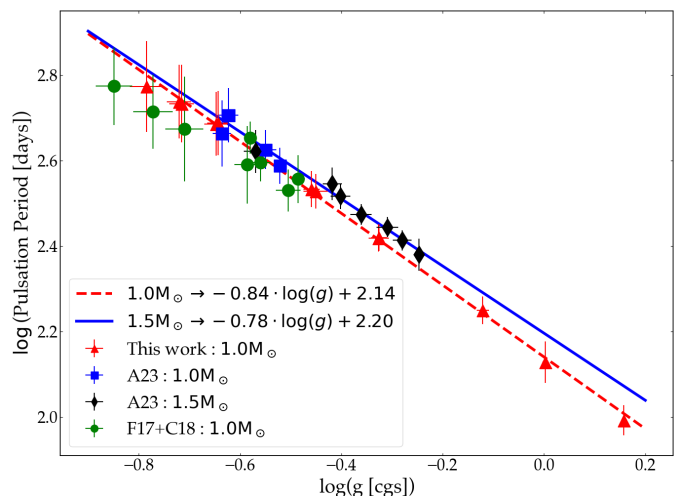


Fig. 2. Log-log plot of the pulsation period [days] versus the surface gravity, g [cgs], which follows a linear law whose parameters were computed with a non-linear least-squares method, given in Eqs. (1) and (2).

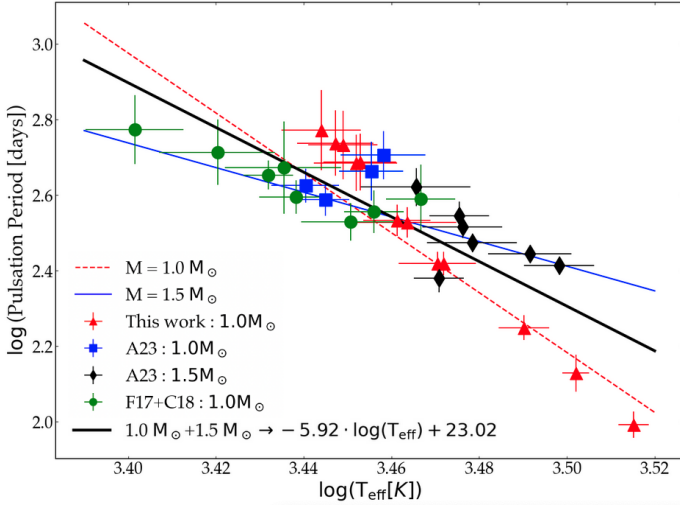


Fig. 3. Log-log plot of the pulsation period [days] versus the effective temperature, T_{eff} [K], which is in agreement with photosphere dynamics. We notice two groups of data (above and below the black curve) that are not linked to mass. The linear relation is given in Eq. (3).

We compared the pulsation period, P_{puls} , with the effective temperature, T_{eff} . Ahmad et al. (2023) showed that the pulsation period decreases when the temperature increases. A linear correlation is confirmed with our simulations, as is displayed in Fig. 3. However, we do not see any clear differentiation between the law found from the $1.0 M_{\odot}$ simulations and the law from the $1.5 M_{\odot}$ simulations so we chose to use all simulations to infer a law between P_{puls} and T_{eff} (Eq. (3) and the black curve in Fig. 3). We computed the reduced $\chi^2 = 77$ and the parameters of the linear law are expressed as follows:

$$\log(P_{\text{puls}}) = -5.92 \cdot \log(T_{\text{eff}}) + 23.02. \quad (3)$$

Ahmad et al. (2023) found a correlation between the pulsation period and the inverse square root of the stellar mean-density (M_{\star}/R_{\star}^3 , see Eq. (4) in the aforementioned article). In agreement with this study, we found a linear correlation between $\log(P_{\text{puls}})$ and $\log(R_{\star})$, with R_{\star} the stellar radius (Fig. 4). We computed with the least-squares method $\bar{\chi}_{1.0}^2 = 2.0$ and $\bar{\chi}_{1.5}^2 = 0.4$ and the parameters of the linear law are expressed as follows:

$$\log(P_{\text{puls}}) = 1.68 \cdot \log(R_{\star}) - 1.59, \quad \text{for } M_{\star} = 1.0 M_{\odot} \quad (4)$$

$$\log(P_{\text{puls}}) = 1.54 \cdot \log(R_{\star}) - 1.36, \quad \text{for } M_{\star} = 1.5 M_{\odot}. \quad (5)$$

We compared our results with the relation found by Vassiliadis & Wood (1993) — $\log(P_{\text{puls}}) = -2.07 + 1.94 \log(R_{\star}/R_{\odot}) - 0.9 \log(M_{\star}/M_{\odot})$ — and with the fundamental mode of long-period variables, Eq. (12), found by Trabucchi et al. (2019) (see Figs. 5 and 6). We used the solar metallicity and helium mass function from Asplund et al. (2009) and the reference carbon-to-oxygen ratio from Trabucchi et al. (2019). Overall, we have the same trends, but we notice that the laws we obtained are less steep than the relation from Vassiliadis & Wood (1993) and the fundamental mode from Trabucchi et al. (2019), meaning that the pulsation periods of our simulations are shorter than expected.

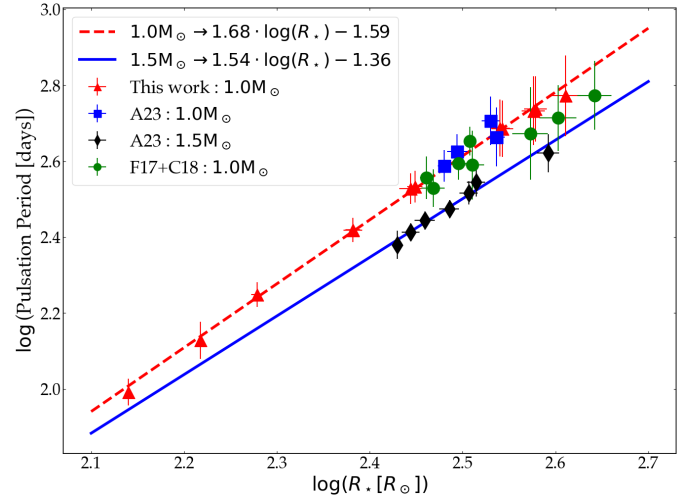


Fig. 4. Log-log of the pulsation period [days] versus the stellar radius R_{\star} [R_{\odot}], which is in agreement with photosphere dynamics. The linear laws' expressions are given in Eqs. (4) and (5).

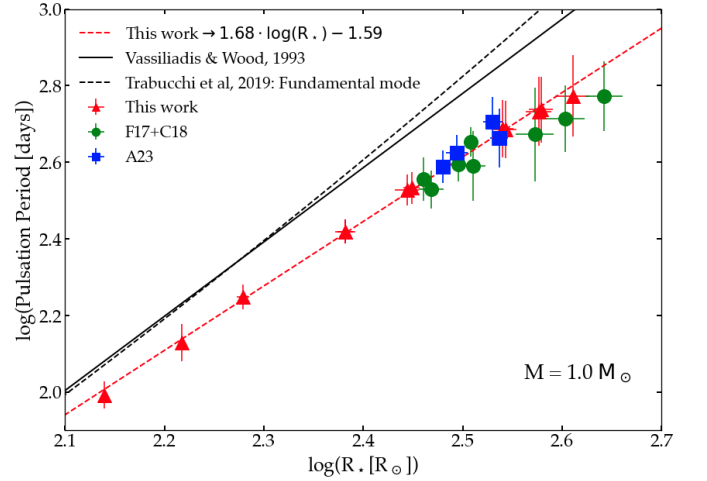


Fig. 5. Case of the $1.0 M_{\odot}$ simulations: Log-log of the pulsation period [days] versus the stellar radius, R_{\star} [R_{\odot}]. We compare the analytical law established here (dashed red curve) with the law from Vassiliadis & Wood (1993) (black curve) and with the fundamental mode from Trabucchi et al. (2019) (dashed black curve). Overall, we found similar trends, only separated by an offset. The pulsation periods of the simulations are shorter than expected.

2.3. Photocentre variability of the RHD simulations in the *Gaia* G band

For each intensity map computed (for example, Fig. 7), we calculated the position of the photocentre as the intensity-weighted mean of the x-y positions of all emitting points tiling the visible stellar surface according to

$$P_x = \frac{\sum_{i=1}^N \sum_{j=1}^N I(i, j) \cdot x(i, j)}{\sum_{i=1}^N \sum_{j=1}^N I(i, j)} \quad (6)$$

$$P_y = \frac{\sum_{i=1}^N \sum_{j=1}^N I(i, j) \cdot y(i, j)}{\sum_{i=1}^N \sum_{j=1}^N I(i, j)}, \quad (7)$$

where $I(i, j)$ is the emerging intensity for the grid point (i, j) with co-ordinates $x(i, j), y(i, j)$ and N the number of points in each co-ordinate of the simulated box.

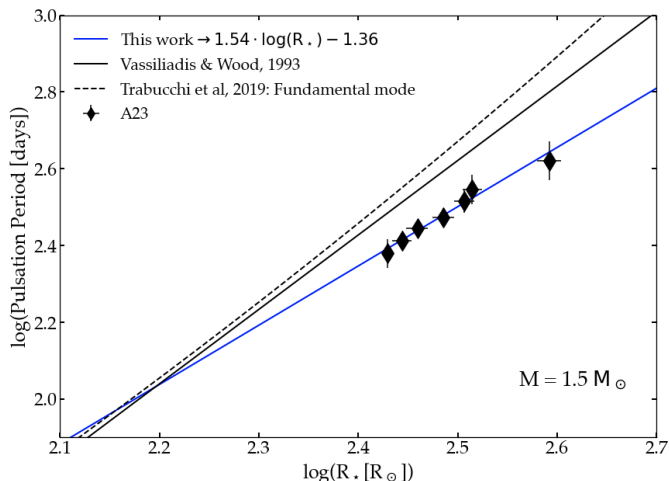


Fig. 6. Case of the $1.5 M_{\odot}$ simulations: Same as in Fig. 5. In this case, the mass appears in the equations from Trabucchi et al. (2019) as its logarithm does not equal zero anymore.

Large-scale convective cells drag hot plasma from the core towards the surface, where it cools down and sinks (Freytag et al. 2017). Coupled with pulsations, this causes optical depth and brightness temporal and spatial variability, moving the photocentre position (Chiavassa et al. 2011, 2018). Thus, in the presence of brightness asymmetries, the photocentre will not coincide with the barycentre of the star. Figure 7 displays the time variability of the photocentre position (blue star) for three snapshots of the simulation *st28gm05n028*. The dashed lines intersect at the geometric centre of the image.

We computed the time-averaged photocentre position, $\langle P_x \rangle$ and $\langle P_y \rangle$, for each Cartesian co-ordinate in astronomical units, [AU], the time-averaged radial photocentre position, $\langle P \rangle$ as $\langle P \rangle = (\langle P_x \rangle^2 + \langle P_y \rangle^2)^{1/2}$, and its standard deviation, σ_P , in AU and as a percentage of the corresponding stellar radius, R_{\star} [% of R_{\star}] (see Table A.1).

Figure 8 displays the photocentre displacement over the total duration for the simulation *st28gm05n028*, with the average position as the red dot and σ_P as the red circle radius (see additional simulations in Figs. B1 to B21, available on Zenodo²).

We also computed the histogram of the radial position of the photocentre for every snapshot available of every simulation (Fig. 9). The radial position is defined as $P = (P_x^2 + P_y^2)^{1/2}$ in % of R_{\star} . We notice that the photocentre is mainly situated between 0.05 and 0.15 of the stellar radius.

2.4. Correlation between the photocentre displacement and the stellar parameters

After the correlations between P_{puls} and the stellar parameters ($\log(g)$, T_{eff} and R_{\star}), we studied correlations between P_{puls} and the photocentre displacement, σ_P , displayed in Fig. 10. The pulsation period increases when the surface gravity decreases (Fig. 2); in other words, when the stellar radius increases. The photocentre gets displaced across larger distances (Chiavassa et al. 2018). We notice a correlation for each sub-group that we approximated with a power law, whose parameters were determined with a non-linear least-squares method (see Eq. (8) and (9)):

$$\log(P_{\text{puls}}) = 3.38 \cdot x^{0.12}, \quad \text{with } x = \sigma_P \text{ or } x = \sigma_{\varpi} \quad (8)$$

$$\log(P_{\text{puls}}) = 3.44 \cdot x^{0.13}, \quad \text{with } x = \sigma_P \text{ or } x = \sigma_{\varpi}. \quad (9)$$

The resulting reduced $\bar{\chi}^2$ are $\bar{\chi}_{1.0}^2 \sim 161$ and $\bar{\chi}_{1.5}^2 \sim 2$. As before, we note a stark difference because there are fewer $1.5 M_{\odot}$ simulations and they are less scattered.

3. Comparison with observations from the *Gaia* mission

From the RHD simulations, we found analytical laws between the pulsation period and stellar parameters and between the pulsation period and the photocentre displacement, which were used to estimate the uncertainties of the results. We used these laws with the parallax uncertainty, σ_{ϖ} , measured by *Gaia* to derive the stellar parameters of observed stars.

3.1. Selection of the sample

To compare the analytical laws with observational data, the parameters of the observed stars need to match the parameters of the simulations. Uttenthaler et al. (2019) investigated the interplay between mass-loss and third dredge-up (3DUP) of a sample of variable stars in the solar neighbourhood, which we further constrained to select suitable stars for our analysis by following these conditions: (i) Mira stars with an assumed solar metallicity, (ii) a luminosity, L_{\star} , lower than $10000 L_{\odot}$, and $\sigma_{L_{\star}}/L_{\star} < 50\%$, $\sigma_{L_{\star}}$ being the uncertainty on the luminosity, and (iii) the GDR3 parallax uncertainty, σ_{ϖ} , lower than 0.14 mas. We also selected stars whose (iv) renormalised unit weight error (RUWE) is lower than 1.4 (Andriantsaralaza et al. 2022). This operation resulted in a sample of 53 Mira stars (Table A.2).

The pulsation periods were taken mainly from Templeton et al. (2005) where available, or were also collected from VizieR. Preference was given to sources with available light curves that allowed for a critical evaluation of the period, such as the All Sky Automated Survey (Pojmanski 1998). Since some Miras have pulsation periods that change significantly in time (Wood & Zarro 1981; Templeton et al. 2005), we also analysed visual photometry from the AAVSO³ database and determined present-day periods with the program Period04⁴ (Lenz & Breger 2005). The analysis of Merchan-Benitez et al. (2023) provided a period variability of the order of 2.4% of the respective pulsation period for Miras in the solar neighbourhood.

The luminosities were determined from a numerical integration under the photometric spectral energy distribution between the B-band at the short end and the IRAS $60 \mu\text{m}$ band or, if available, the Akari $90 \mu\text{m}$ band. A linear extrapolation to $\lambda = 0$ and $\nu = 0$ was taken into account. The photometry was corrected for interstellar extinction using the map of Gontcharov (2017). We adopted the GEDR3 parallaxes and applied the average zero-point offset of quasars found by Lindegren et al. (2021): -21 mas . Two main sources of uncertainty on the luminosity are the parallax uncertainty and the intrinsic variability of the stars. The uncertainty on interstellar extinction and on the parallax zero-point were neglected.

³ <https://www.aavso.org/>

⁴ <http://period04.net/>

² <https://zenodo.org/records/12802110>

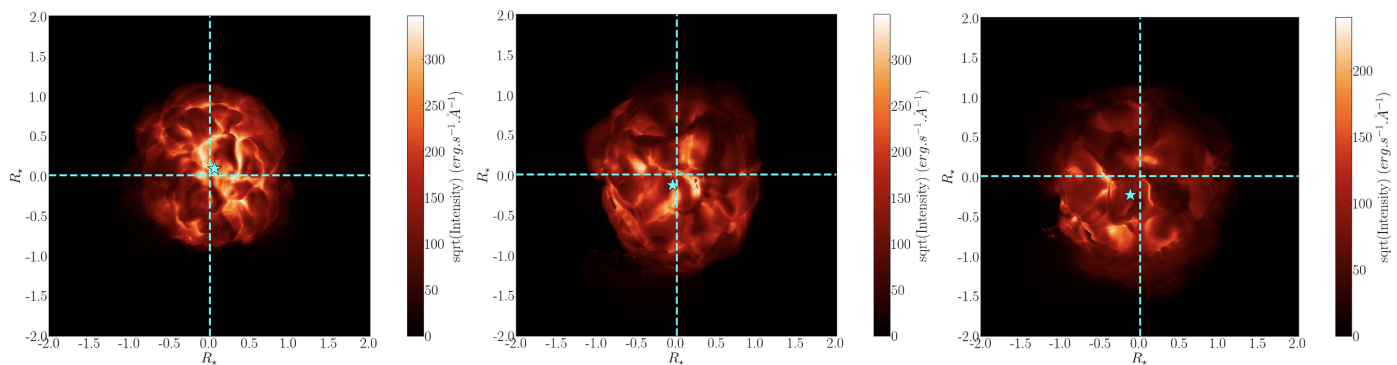


Fig. 7. Temporal evolution of an AGB simulation. The intensity maps are in $\text{erg} \cdot \text{s}^{-1} \cdot \text{\AA}^{-1}$. The star indicates the position of the photocentre at the given time for the simulation *st28gm05n028*. The dashed lines intersect at the geometric centre of the image.

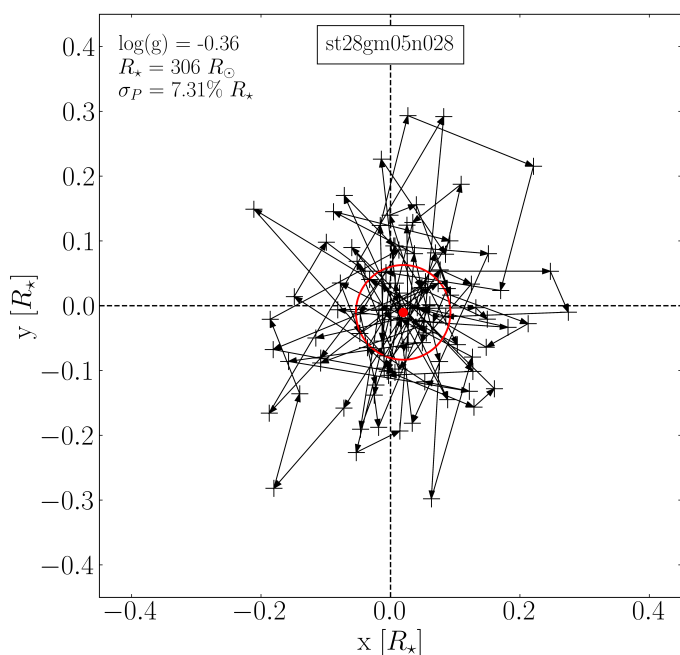


Fig. 8. Temporal evolution of the photocentre displacement for an AGB simulation, here *st28gm05n028*, same as in Fig. 7. The dashed lines intersect at the geometric centre of the image. The red dot indicates the average position of the photocentre and the red circle its standard deviation.

The RUWE⁵ is expected to be around 1.0 for sources where the single-star model provides a good fit to the astrometric observations. Following Andriantsaralaza et al. (2022), we rejected stars whose RUWE is above 1.4 as their astrometric solution is expected to be poorly reliable and may indicate unresolved binaries.

Figure 11 displays the location of stars in a pulsation period-luminosity diagram with the colour scale indicating the number of good along-scan observations — that is, *astrometric_n_good_obs_al* data from GDR3 (top panel) — or indicating the RUWE (bottom panel). We investigated whether the number of times a star is observed, N_{obs} , or the number of observed periods, N_{per} , is correlated with RUWE. We do not see improvements of the astrometric solution when more observations are used to compute it.

⁵ <https://gea.esac.esa.int/archive/documentation/GDR2/>, Part V, Chapter 14.1.2

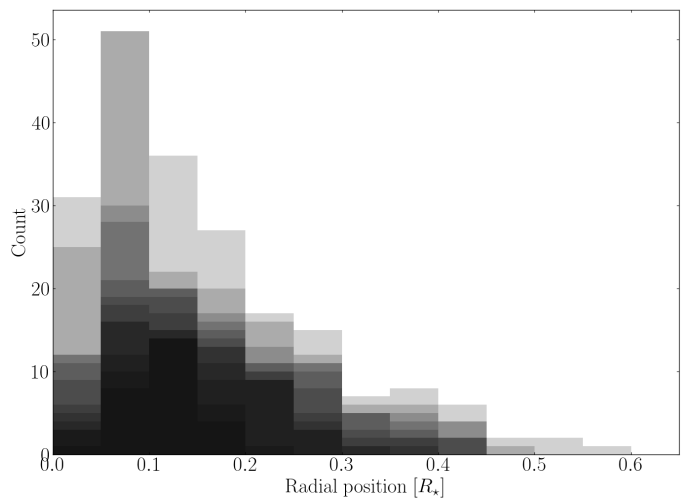


Fig. 9. Histograms of the radial positions of the photocentre for all the intensity maps we computed and used in this work. The darker the shadow, the more often the photocentre is situated in the associated bin. Overall, we notice the photocentre is situated between 5% and 15% of the stellar radius.

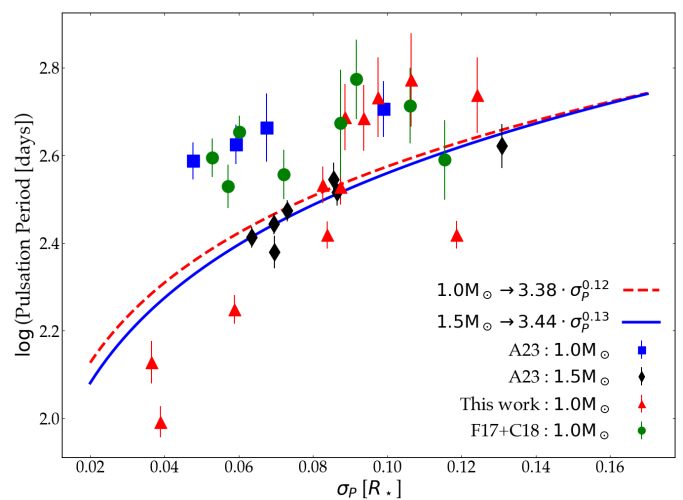


Fig. 10. Pulsation period in logarithmic scale versus the photocentre displacement for the 31 models. We group the models whether their mass is equal to $1.0 M_{\odot}$ or $1.5 M_{\odot}$. We approximate our data by a power law, one for each group (see Eq. (8), (9)).

Information about the third dredge-up activity of the stars is available from spectroscopic observations of the absorption

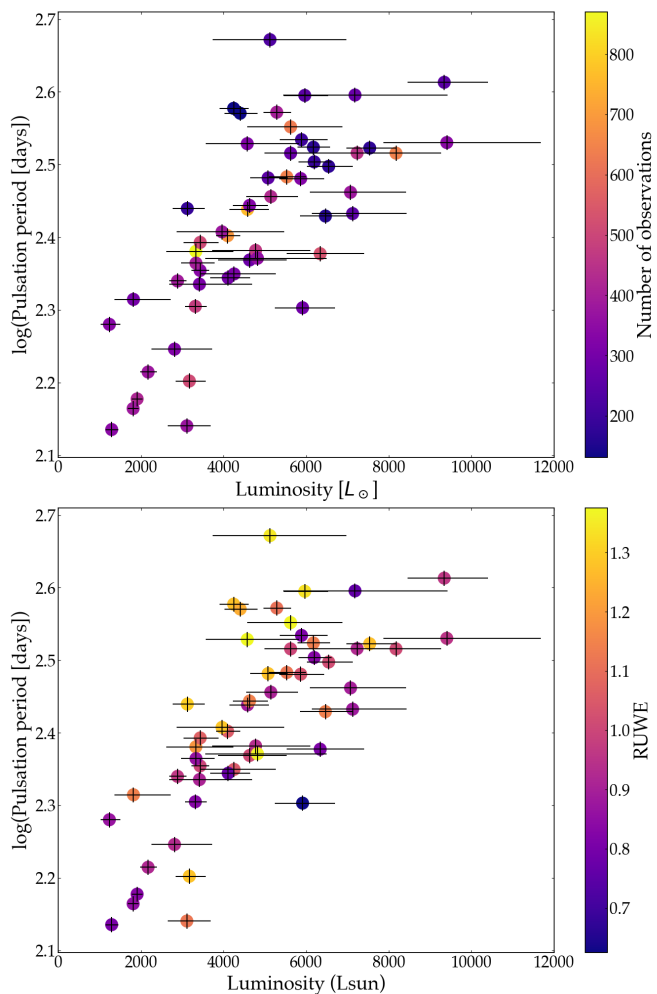


Fig. 11. Pulsation period in logarithmic scale [days] of the sample versus their luminosity, $[L_{\odot}]$. **Top panel:** Number of observations in colour scale. **Bottom panel:** RUWE in colour scale.

lines of technetium (Tc, see Uttenthaler et al. 2019). Tc-rich stars have undergone a third dredge-up event and are thus more evolved and/or more massive than Tc-poor stars. Also, since ^{12}C is dredged up along with Tc, the C/O ratio could be somewhat enhanced in the Tc-rich compared to the Tc-poor stars. However, as our subsequent analysis showed, we do not find significant differences between Tc-poor and Tc-rich stars with respect to their astrometric characteristics; hence, this does not impact our results.

3.2. Origins of the parallax uncertainty

The uncertainty in *Gaia* parallax measurements has multiple origins: (i) instrumental (Lindgren et al. 2021), (ii) distance (Lindgren et al. 2021), and (iii) convection-related (Chiavassa et al. 2011, 2018, 2022). This makes the error budget difficult to estimate. In particular, only with time-dependent parallaxes with *Gaia* Data Release 4 will the convection-related part be definitively characterised (Chiavassa et al. 2019). Concerning the distance and instrumental parts, Lindgren et al. (2021) investigated the bias of the parallax versus magnitude, colour, and position and developed an analytic method to correct the parallax of these biases. For comparison, the parallax and the corrected parallax are displayed in Table A.2, columns 8 and 9, respectively. In this work, we assume that convective-related variability is the main

contributor to the parallax uncertainty budget, which is already hinted at in observations; thus, σ_P is equivalent to σ_{σ} .

Indeed, optical interferometric observations of an AGB star showed the presence of large convective cells that affected the photocentre position. It has been shown for the same star that the convection-related variability accounts for a substantial part of the *Gaia* Data Release 2 parallax error (see in particular Fig. 2, Chiavassa et al. 2020).

3.3. Retrieval of the surface gravity based on the analytical laws

In Section 2.4, we established an analytical law, Eq. (8), between σ_P and P_{puls} with the $1.0 M_{\odot}$ simulations. We used it to calculate the pulsation period, $P_{1.0}$, of the stars from observed σ_{σ} . We defined $\Delta P_{1.0}$, the relative difference between the observed pulsation period, P_{obs} , and our results as $\Delta P_{1.0} = \frac{P_{\text{obs}} - P_{1.0}}{P_{\text{obs}}}$. This intermediate step gives an estimation of the error when computing the pulsation period and comparing it with observations. This error can then be used as a guideline to estimate the uncertainties of the final results; in other words, of the effective temperature, the surface gravity, and the radius of the stars in our sample.

The top panel of Figure 12 displays P_{obs} versus σ_{σ} as dots and $P_{1.0}$ versus σ_{σ} as the dashed red curve. The bottom panel displays the histogram of the relative difference, $\Delta P_{1.0}$, and the cumulative percentage of the observed sample. The same colour scale is used in both panels: for example, light yellow represents a relative difference between $P_{1.0}$ and P_{obs} of less than 5%, while purple represents a relative difference greater than 60% (column 3 in Table A.3).

$\Delta P_{1.0}$ ranges from 0.4% to 72%, with a median of 16% (i.e. from 1 to 68 days' difference). For 85% of the sample stars, $\Delta P_{1.0}$ is $\leq 30\%$, and for 57%, it is $\leq 20\%$, suggesting we statistically have a good agreement between our model results and the observations.

We then combined Eqs. (8) and (1) to derive the surface gravity ($\log(g_{1.0})$) directly from σ_{σ} (column 6 in Table A.3). The top left panel of Figure 14 displays $\log(P_{\text{obs}})$ versus $\log(g_{1.0})$ and Eq. (1) as the dashed red curve. We notice that the calculated $\log(g_{1.0})$ values follow the same trend as $\log(g)$ from the simulations and are the most accurate when closest to the line.

We performed the same analysis with the analytical laws from the $1.5 M_{\odot}$ simulations. The top panel of Figure 13 displays the calculated $P_{1.5}$ versus σ_{σ} and the bottom panel displays a histogram of the relative difference between $P_{1.5}$ and P_{obs} defined as $\Delta P_{1.5}$ (column 5 in Table A.3). The same colour code is used in both panels. We combined Eqs. (9) and (2) to compute $\log(g_{1.5})$. Fig. 14 displays $\log(P_{\text{obs}})$ from the simulations versus $\log(g_{1.5})$.

For the $1.5 M_{\odot}$ simulations, $\Delta P_{1.5}$ ranges from 0.6% to 62%, with a median of 16% (i.e. from 1 to 76 days' difference). For 81% of the sample stars, $\Delta P_{1.5}$ is $\leq 30\%$, and for 70%, it is $\leq 20\%$.

Qualitatively, we observe two different analytical laws depending on the mass of the models used to infer the laws. However, a larger grid of simulations, covering the mass range of AGB stars, would help to confirm this trend, tailor the analytical laws to specific stars, and predict more precise stellar parameters.

3.4. Retrieval of the other stellar parameters

We repeated the same procedure to retrieve the stellar radius, $R_{1.0}$, and the effective temperature, $T_{1.0}$ (columns 8 and 10 in

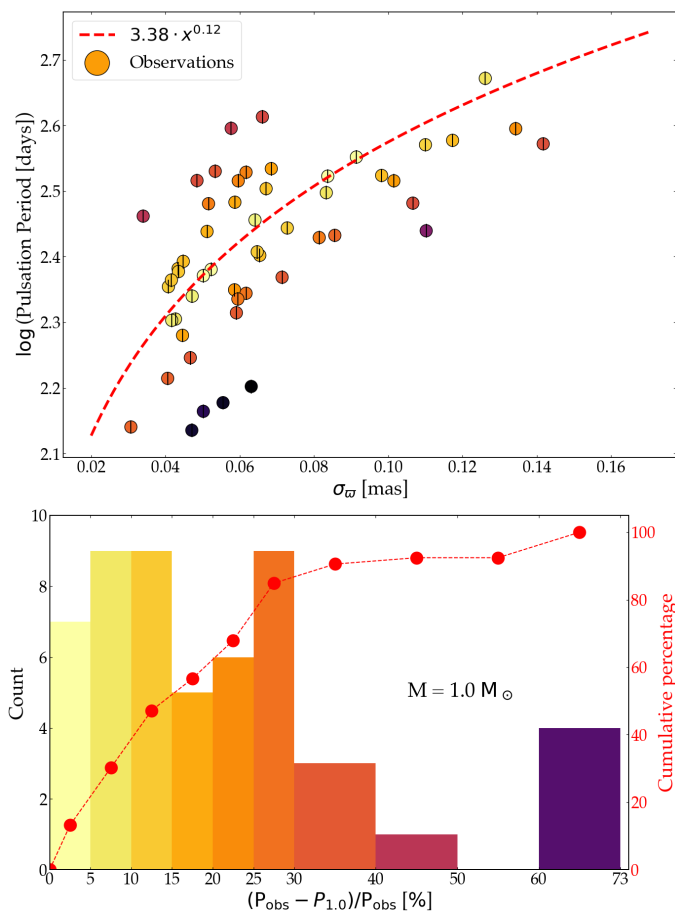


Fig. 12. Comparison of the pulsation period of the sample between observations and estimations from the simulations where $M_{\star} = 1.0 M_{\odot}$. **Top panel:** Pulsation period, P_{obs} , in logarithmic scale versus the parallax uncertainty of the observed sample, the dashed red curve being the Eq. (8) inferred from the analysis of the $1.0 M_{\odot}$ simulations. The colours represent the relative difference between the pulsation period calculated from Eq. (8) and the observations. **Bottom panel:** Histogram of these relative differences. The red line accounts for the cumulative number of stars in the respective and preceding bins (see right-hand Y-axis). The limits of the last bin are 60% and 73%, with only one star above 70%

Table A.3). Combining Eqs. (8) and (4), we computed the radius, $R_{1.0}$. The top central panel of Figure 14 displays $\log(P_{\text{obs}})$ versus $\log(R_{1.0})$. Combining the Eqs. (8) and (3), we computed the effective temperature, $T_{1.0}$ (Fig. 14, top right panel). As in Section 3.3 for $\log(g_{1.0})$, the calculated $\log(R_{1.0})$ follow the Eq. 4 derived from the simulations, and $\log(R_{1.0})$ follow Eq. 3.

We repeated the same procedure for the $1.5 M_{\odot}$ simulations to retrieve $R_{1.5}$ and $T_{1.5}$ (columns 9 and 11 in Table A.1). The results are displayed in the bottom central and right panels of Fig. 14.

For comparison, R Peg has been observed with the interferometric instrument GRAVITY/VLTI in 2017, which provided a direct estimation of its radius: $R_{\text{Ross}} = 351^{+38}_{-31} R_{\odot}$ (Witkowski et al. 2018). From our study, $R_{1.0, \text{RPeg}} = 321^{+5}_{-15} R_{\odot}$ and $R_{1.5, \text{RPeg}} = 373^{+5}_{-14} R_{\odot}$, which is in good agreement with the results of Witkowski et al. (2018). With future interferometric observations, we shall be able to further validate our results.

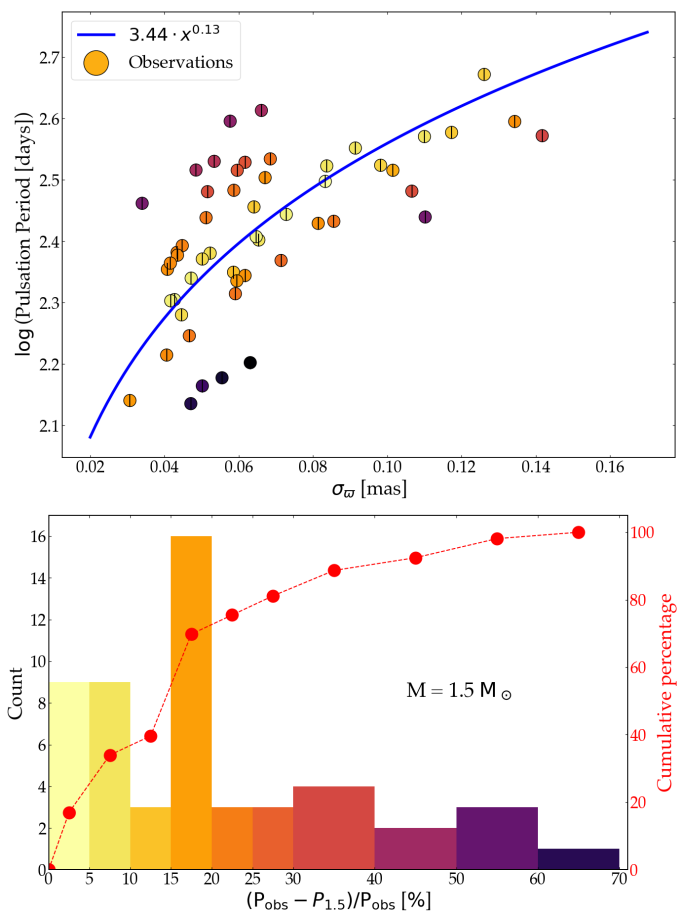


Fig. 13. Comparison of the pulsation period of the sample between observations and estimations from the simulations where $M_{\star} = 1.5 M_{\odot}$. **Top panel:** Pulsation period, P_{obs} , in logarithmic scale versus the parallax uncertainty of the observed sample, the blue curve being the Eq. (9) inferred from the analysis of the $1.5 M_{\odot}$ simulations. The colours represent the relative difference between the pulsation period calculated from Eq. (9) and with the observations. **Bottom panel:** Histogram of these relative differences. The red line accounts for the cumulative number of stars in the respective and preceding bins (see right-hand Y-axis).

4. Summary and conclusions

We computed intensity maps in the *Gaia* band from the snapshots of 31 RHD simulations of AGB stars computed with CO⁵BOLD. The standard deviation of the photocentre displacement, σ_P , due to the presence of large convective cells on the surface, ranges from about 4% to 13% of its corresponding stellar radius, which is coherent with previous studies and is non-negligible in photometric data analysis. It becomes the main contributor to the *Gaia* parallax uncertainty σ_{π} budget. The dynamics and winds of the AGB stars also affect the determination of stellar parameters and amplify their uncertainties. It becomes worth exploring the correlations between all these aspects to eventually retrieve such parameters from the parallax uncertainty.

We provided correlations between the photocentre displacement and the pulsation period as well as between the pulsation period and stellar parameters: the effective surface gravity, $\log(g)$, the effective temperature, T_{eff} , and the radius, R_{\star} . We separated the simulations into two sub-groups based on whether their mass is equal to 1.0 or $1.5 M_{\odot}$. Indeed, the laws we provided, and the final results, are sensitive to the mass. A grid of simulations covering a larger range of masses, with a meaningful

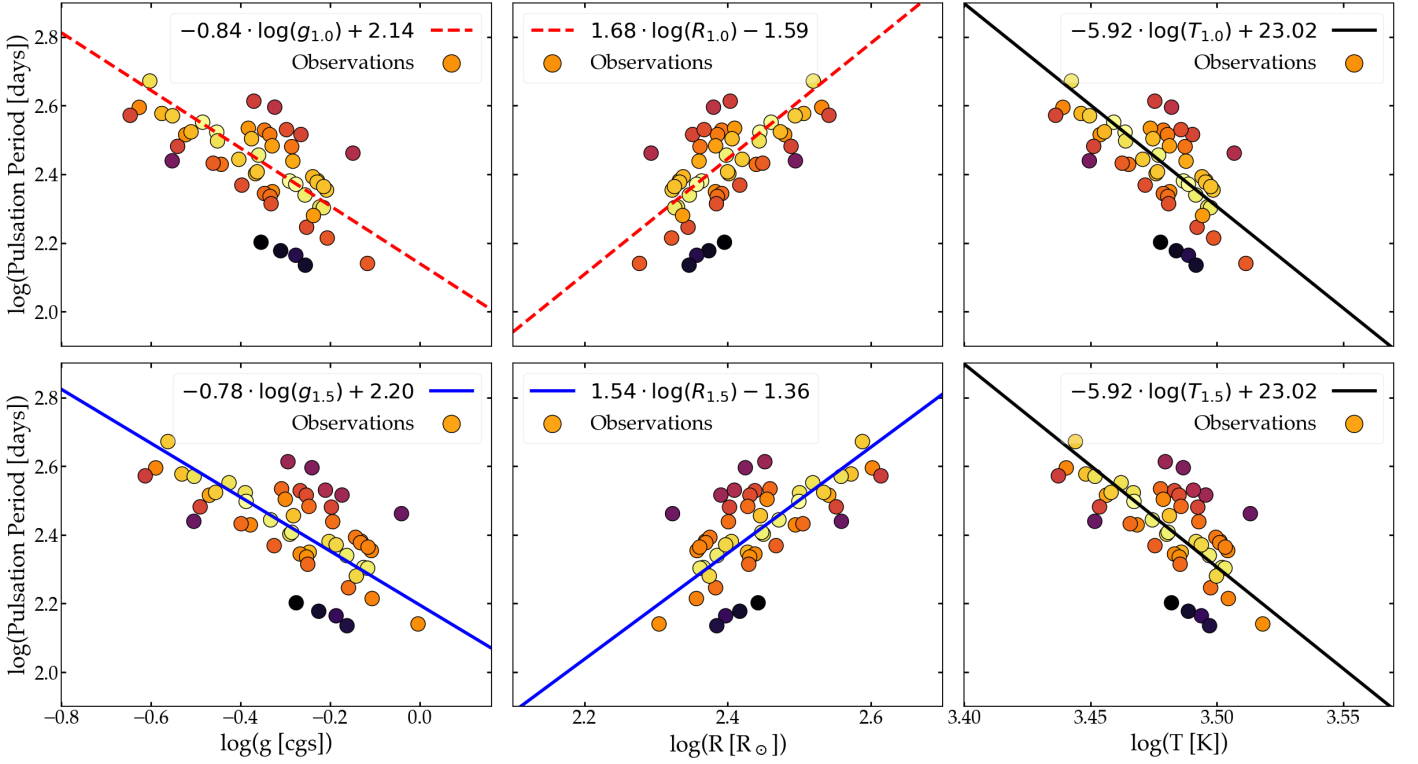


Fig. 14. Pulsation period from the observations versus stellar parameter values obtained from the simulations. **Top row:** Pulsation period versus $\log(g)$ (left column), $\log(R_{\star})$ (central column), $\log(T_{\text{eff}})$ (right column), each computed thanks to the analytical laws derived from the $1.0 M_{\odot}$ simulations. **Bottom row:** Same as in the top row for the $1.5 M_{\odot}$ simulations. The equation of each law is given in the legend and is reported in Fig. 15. The colour scale used is the same as in Figs. 12 and 13.

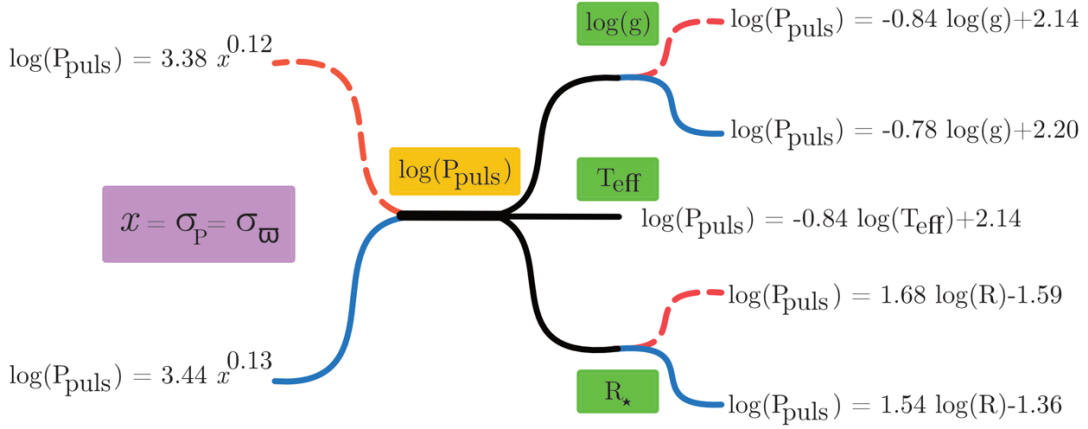


Fig. 15. Summary of the analytical laws we established. The dashed red lines correspond to the analysis when using only the $1.0 M_{\odot}$ simulations, the blue lines the analysis when using only the $1.5 M_{\odot}$ simulations. For the correlation between the pulsation period and the effective temperature, all available simulations were used. In the left part, we have the laws between the photocentre displacement and the pulsation period from the simulations. We assume that the parallax uncertainty, σ_{π} , is equivalent to σ_P as σ_P is the main contributor of the σ_{π} budget. In the right part, we have the laws between the pulsation period and the stellar parameters ($\log(g)$, T_{eff} , R_{\star}). Combining these laws provides the parameters of the Mira stars based on the parallax uncertainty. The relative difference between the calculated and the observational pulsation periods can be used to estimate the uncertainties of the stellar parameters.

number of simulations for each, would help confirm this observation and establish laws that are suitable for varied stars. This will be done in the future.

We then applied these laws to a sample of 53 Mira stars matching the simulations' parameters. We first compared the pulsation period with the literature: we obtained a relative error of less than 30% for 85% of the stars in the sample for the first case and 81% for the second, which indicates reasonable results

from a statistical point of view. This error can then be used as a guideline to estimate the uncertainties of the final results. We then computed $\log(g)$, T_{eff} and R_{\star} by combining the analytical laws (Table A.3).

While mass loss from red giant branch stars should be mainly independent of metallicity, it has been suggested that this is less true for AGB stars (McDonald & Zijlstra 2015). Photocentre dis-

placement and stellar parameters may be dependent on metallicity and this question needs to be further studied.

We argue that the method used for Mira stars presented in this article, based on RHD simulations, can be generalised to any AGB stars whose luminosity is in the 2000–10000 L_{\odot} range and that have a *Gaia* parallax uncertainty below 0.14 mas. Figure 15 sums up the analytical laws found in this work that can be used to calculate the stellar parameters.

Overall, we have demonstrated the feasibility of retrieving stellar parameters for AGB stars using their uncertainty on the parallax, thanks to the employment of state-of-the-art 3D RHD simulations of stellar convection. The future *Gaia* Data Release 4 will provide time-dependent parallax measurements, allowing one to quantitatively determine the photocentre-related impact on the parallax error budget and to directly compare the convection cycle, refining our understanding of AGB dynamics.

Acknowledgements. This work is funded by the French National Research Agency (ANR) project PEPPER (ANR-20-CE31-0002). BF acknowledges funding from the European Research Council (ERC) under the European Union's Horizon 2020 research and innovation programme Grant agreement No. 883867, project EXWINGS. The computations were enabled by resources provided by the Swedish National Infrastructure for Computing (SNIC). This work was granted access to the HPC resources of Observatoire de la Côte d'Azur - Mésocentre SIGAMM.

References

- Ahmad, A., Freytag, B., & Höfner, S. 2023, *A&A*, 669, A49
- Andriantsaralaza, M., Ramstedt, S., Vlemmings, W. H. T., & De Beck, E. 2022, *A&A*, 667, A74
- Asplund, M., Grevesse, N., Sauval, A. J., & Scott, P. 2009, *ARA&A*, 47, 481
- Chen, D.-C., Xie, J.-W., Zhou, J.-L., et al. 2021, *ApJ*, 909, 115
- Chiavassa, A., Freytag, B., & Schultheis, M. 2018, *A&A*, 617, L1
- Chiavassa, A., Freytag, B., & Schultheis, M. 2019, Proceedings of the Annual meeting of the French Society of Astronomy and Astrophysics
- Chiavassa, A., Kravchenko, K., Millour, F., et al. 2020, *A&A*, 640, A23
- Chiavassa, A., Kudritzki, R., Davies, B., Freytag, B., & de Mink, S. E. 2022, *A&A*, 661, L1
- Chiavassa, A., Pasquato, E., Jorissen, A., et al. 2011, *A&A*, 528, A120
- Chiavassa, A., Plez, B., Josselin, E., & Freytag, B. 2009, *A&A*, 506, 1351
- De Beck, E., Decin, L., de Koter, A., et al. 2010, *A&A*, 523, A18
- Decin, L. 2021, *ARA&A*, 59, 337
- Freytag, B. 2013, *Mem. Soc. Astron. Ital. Suppl.*, 24, 26
- Freytag, B. 2017, *Mem. Soc. Astron. Ital.*, 88, 12
- Freytag, B., Holweger, H., Steffen, M., & Ludwig, H. G. 1997, Proceedings of the ESO Workshop, 316
- Freytag, B. & Höfner, S. 2023, *A&A*, 669, A155
- Freytag, B., Liljegren, S., & Höfner, S. 2017, *A&A*, 600, A137
- Freytag, B., Steffen, M., Ludwig, H. G., et al. 2012, *J. Comput. Phys.*, 231, 919
- Gaia Collaboration, Prusti, T., de Bruijne, J. H. J., et al. 2016, *A&A*, 595, A1
- Gaia Collaboration, Vallenari, A., Brown, A. G. A., et al. 2023, *A&A*, 674, A1
- Gontcharov, G. A. 2017, *Astronomy Letters*, 43, 472
- Gustafsson, B., Edvardsson, B., Eriksson, K., et al. 2008, *A&A*, 486, 951
- Höfner, S. & Olofsson, H. 2018, *A&A Rev.*, 26, 1
- Lenz, P. & Breger, M. 2005, *Communications in Asteroseismology*, 146, 53
- Lindgren, L., Bastian, U., Biermann, M., et al. 2021, *A&A*, 649, A4
- McDonald, I. & Zijlstra, A. A. 2015, *MNRAS*, 448, 502
- Merchan-Benitez, P., Uttenthaler, S., & Jurado-Vargas, M. 2023, *A&A*, 672, A165
- Pojmanski, G. 1998, *Acta Astronomica*, 48, 35
- Templeton, M. R., Mattei, J. A., & Willson, L. A. 2005, *AJ*, 130, 776
- Trabucchi, M., Wood, P. R., Montalbán, J., et al. 2019, *MNRAS*, 482, 929
- Uttenthaler, S., McDonald, I., Bernhard, K., Cristallo, S., & Gobrecht, D. 2019, *A&A*, 622, A120
- Vassiliadis, E. & Wood, P. R. 1993, *ApJ*, 413, 641
- Wittkowski, M., Rau, G., Chiavassa, A., et al. 2018, *A&A*, 613, L7
- Wood, P. R. & Zarro, D. M. 1981, *ApJ*, 247, 247

Appendix A: Tables

Table A.1. RHD simulation parameters.

Id	Simulation	M_{\star} [M_{\odot}]	L_{\star} [L_{\odot}]	R_{\star} [R_{\odot}]	T_{eff} [K]	$\log g$ [cgs]	t_{avg} [yr]	P_{puls} [days]	$\sigma_{P_{\text{puls}}}$ [days]	$\langle P_x \rangle$ [AU]	$\langle P_y \rangle$ [AU]	σ_P [AU]	σ_P % [R_{\star}]
1	st28gm05n038	1.0	4978	281	2893	-0.46	19.05	341	31	-0.025	-0.004	0.108	8.26
2	st28gm05n043	1.0	5013	278	2908	-0.45	19.03	337	30	-0.011	-0.044	0.113	8.74
3	st28gm06n057	1.0	7055	349	2831	-0.65	15.87	485	77	0.012	0.005	0.152	9.37
4	st28gm06n059	1.0	7050	347	2837	-0.64	15.87	487	77	0.082	-0.055	0.143	8.86
5	st28gm07n006	1.0	8003	379	2801	-0.72	15.85	546	99	-0.055	0.011	0.219	12.43
6	st28gm07n008	1.0	8020	377	2812	-0.72	15.84	541	102	0.006	-0.029	0.171	9.75
7	st28gm08n001	1.0	8980	408	2780	-0.78	19.39	592	129	-0.141	-0.018	0.202	10.65
8	st29gm02n013	1.0	2983	190	3092	-0.12	11.23	178	13	-0.015	-0.012	0.052	5.89
9	st29gm03n001	1.0	3990	241	2955	-0.33	15.22	262	18	0.001	-0.001	0.094	8.39
10	st29gm03n002	1.0	4028	241	2964	-0.33	15.22	263	18	0.008	-0.008	0.133	11.87
11	st31gm01n002	1.0	2500	165	3177	0.01	9.13	134	14	-0.002	-0.003	0.028	3.65
12	st32g01n002	1.0	1978	138	3275	0.16	7.02	98	8	-0.006	-0.007	0.025	3.90
13	st28gm05n006	1.5	4985	269	2957	-0.25	15.85	240	20	-0.003	0.004	0.087	6.95
14	st28gm05n008	1.0	4942	302	2786	-0.52	15.85	387	36	0.003	-0.032	0.067	4.77
15	st28gm05n017	1.5	7490	321	2994	-0.40	15.86	328	22	-0.013	-0.072	0.129	8.64
16	st28gm05n020	1.5	7708	327	2989	-0.42	15.86	351	30	-0.046	-0.023	0.130	8.55
17	st28gm05n022	1.0	5068	312	2757	-0.55	15.85	422	42	0.005	-0.027	0.086	5.93
18	st28gm05n028	1.5	6946	306	3009	-0.36	15.85	298	16	0.028	-0.015	0.104	7.31
19	st28gm05n029	1.5	6941	288	3102	-0.31	15.70	278	15	0.024	-0.010	0.093	6.94
20	st28gm05n034	1.5	6880	278	3150	-0.28	7.93	259	14	-0.004	-0.040	0.082	6.34
21	st28gm06n032	1.0	7062	339	2872	-0.62	15.87	508	69	-0.034	0.011	0.156	9.90
22	st28gm06n043	1.0	7079	344	2854	-0.64	15.87	461	75	-0.062	-0.041	0.108	6.75
23	st28gm06n053	1.5	10073	391	2922	-0.57	15.85	418	46	0.009	-0.068	0.238	13.09
24	st26gm07n002	1.0	6986	439	2524	-0.85	25.35	594	112	-0.100 ^a	0.046 ^a	0.187 ^a	9.16 ^a
25	st26gm07n001	1.0	6953	402	2635	-0.77	27.74	517	94	-0.098 ^a	0.024 ^a	0.198 ^a	10.59 ^a
26	st28gm06n026	1.0	6955	372	2737	-0.70	25.35	471	116	-0.068 ^a	-0.002 ^a	0.152 ^a	8.79 ^a
27	st29gm06n001	1.0	6995	324	2929	-0.59	31.70	389	73	-0.098 ^a	0.016 ^a	0.174 ^a	11.55 ^a
28	st27gm06n001	1.0	5011	322	2704	-0.58	31.73	450	38	-0.027	0.027	0.090	6.01
29	st28gm05n002	1.0	4978	314	2742	-0.56	25.35	393	38	-0.002 ^a	0.033 ^a	0.077 ^a	5.27 ^a
30	st28gm05n001	1.0	5019	289	2858	-0.49	31.83	360	44	-0.057	0.017	0.097	7.22
31	st29gm04n001	1.0	4982	295	2827	-0.50	25.35	339	37	-0.002 ^a	0.023 ^a	0.078 ^a	5.69 ^a

Notes: The simulations 1-12 are the new models presented in this work; the simulations 13-23 are presented in Ahmad et al. (2023) and the simulations 24-31 are presented in Freytag et al. (2017) and Chiavassa et al. (2018). The table displays the simulation name, the stellar mass M_{\star} , the average emitted luminosity L_{\star} , the average approximate stellar radius R_{\star} , the effective temperature T_{eff} , the surface gravity $\log(g)$, the pulsation period P_{puls} , the spread in the pulsation period i.e. the pulsation period uncertainty $\sigma_{P_{\text{puls}}}$, and the stellar time t_{avg} used for the averaging of the rest of the quantities. The stellar parameters may slightly vary from original articles as they are updated thanks to Ahmad's and Freytag's work. The last four columns are the time-averaged positions P_x and P_y in AU and the standard deviation of the photocentre displacement σ_P (in AU and in % of R_{\star}). Data denoted by the footnote ^(a) come from the previous analysis of Chiavassa et al. (2018).

Table A.2. Parameters of the sample Miras.

Name	P_{obs} [days]	RUWE	N_{per}	N_{good}	L_{\star} [L_{\odot}]	L_{\star}^{-} [L_{\odot}]	L_{\star}^{+} [L_{\odot}]	ϖ [mas]	ϖ_{corr} [mas]	σ_{ϖ} [mas]	Population
Y And	221	0.774	16	297	4112	431	530	0.557	0.613	0.062	thin
RT Aql	328	1.003	17	277	5623	632	703	1.793	1.844	0.102	thin
SY Aql	356	1.367	22	632	5623	1045	1253	1.067	1.121	0.091	thick
V335 Aql	176	0.931	18	322	2813	561	917	0.191	0.219	0.047	halo
T Aqr	202	0.832	21	479	3317	255	275	0.906	0.960	0.043	thin
U Ari	372	1.240	13	131	4402	381	420	1.674	1.729	0.110	thin
RU Aur	470	1.348	16	230	5125	1387	1847	1.343	1.400	0.126	thin
R Boo	224	1.049	20	314	4255	821	1009	1.520	1.568	0.059	thick
T Cap	271	0.883	12	253	7124	985	1310	0.566	0.624	0.086	thick
CM Car	339	0.955	27	343	9404	1538	2271	0.275	0.294	0.053	thick
U Cet	234	1.011	16	283	4631	764	897	0.954	1.000	0.071	thick
R Cha	338	1.375	24	322	4574	999	1258	1.076	1.102	0.062	thick
S CMi	334	1.138	13	168	6174	378	402	2.393	2.440	0.098	thin
U CMi	410	0.959	15	252	9342	888	1064	0.672	0.723	0.066	thin
W Cnc	394	1.336	15	252	5966	512	571	1.897	1.935	0.134	thin
R Col	328	0.927	28	452	7233	1611	2031	0.696	0.730	0.049	thin
T Col	226	0.998	24	338	3432	211	224	1.603	1.628	0.041	thick
RY CrA	206	1.144	19	302	1819	455	899	0.179	0.193	0.059	thick
X CrB	241	0.934	30	468	4776	1052	1324	0.661	0.708	0.043	thick
R Del	286	0.907	21	430	5144	595	664	1.265	1.318	0.064	thick
W Dra	290	0.897	25	381	7074	980	1350	0.213	0.257	0.034	halo
T Eri	252	1.054	24	690	4099	278	306	1.109	1.146	0.065	thick
U Eri	274	0.890	27	761	4581	433	522	0.516	0.558	0.051	thin
V Gem	275	1.299	14	183	3123	357	421	1.070	1.125	0.110	thin
S Her	304	1.122	18	644	5531	434	466	1.712	1.756	0.059	thin
SV Her	238	0.815	27	531	6339	807	1065	0.306	0.359	0.044	thick
T Her	164	0.923	26	379	2174	195	212	1.153	1.198	0.041	thick
T Hor	219	0.962	28	390	2886	200	217	0.904	0.933	0.047	thick
RR Hya	342	0.811	16	199	5887	528	638	0.710	0.753	0.069	thin
RU Hya	333	1.274	14	176	7538	559	628	1.208	1.261	0.084	thick
S Lac	240	1.188	24	870	3330	717	905	1.254	1.301	0.052	thin
RR Lib	278	1.145	16	329	4629	402	449	1.007	1.062	0.073	thin
R LMi	373	1.106	17	402	5288	327	348	3.446	3.496	0.142	thin
RT Lyn	394	0.761	19	277	7182	1740	2237	0.665	0.722	0.058	thick
U Oct	303	1.034	27	329	5868	518	563	1.009	1.035	0.052	thin
R Oph	303	1.276	16	251	5079	431	470	1.886	1.938	0.107	thick
RY Oph	151	0.829	17	418	1908	129	138	1.324	1.377	0.056	thick
SY Pav	191	0.866	19	338	1237	217	264	0.349	0.348	0.045	thick
R Peg	378	1.276	11	131	4244	336	363	2.629	2.681	0.117	thin
S Peg	314	1.017	13	175	6545	531	583	1.345	1.399	0.083	thick
X Peg	201	0.625	19	290	5913	673	783	0.428	0.483	0.042	thick
Z Peg	328	1.010	18	643	8175	545	581	1.520	1.571	0.060	thin
RZ Sco	159	1.279	16	511	3173	333	391	0.642	0.679	0.063	halo
R Sgr	269	1.146	14	157	6466	610	680	1.138	1.190	0.081	thin
RV Sgr	319	0.830	15	187	6195	383	415	1.306	1.357	0.067	thin
BH Tel	217	0.912	18	311	3417	736	1269	0.220	0.245	0.060	thin
T Tuc	247	1.065	32	509	3435	401	448	0.876	0.911	0.045	thin
RR UMa	231	0.861	29	398	3333	356	450	0.351	0.389	0.042	thick
T UMa	256	1.289	25	378	3963	1103	1503	0.989	1.019	0.065	thick
T UMi	235	1.363	26	355	4821	1258	1673	0.784	0.810	0.050	thick
CI Vel	138	1.121	23	372	3112	457	571	0.223	0.261	0.031	thick
R Vir	146	0.856	15	383	1811	129	138	2.196	2.248	0.050	thin
R Vul	137	0.805	18	340	1292	147	164	1.437	1.488	0.047	thin

Notes: The columns are: Miras' name; the pulsation period P_{obs} obtained from light curves, its uncertainty is assumed to be 2.4% of the corresponding P_{obs} (Merchan-Benitez et al. 2023); RUWE; N_{per} the number of visibility periods used in the astrometric solution⁶, a visibility period consists of a group of observations separated from other groups by at least 4 days. A high number of periods is an indicator of a well-observed source while a value smaller than 10 indicates that the calculated parallax could be more vulnerable to errors (*visibility_periods_used* in the *Gaia* archive); N_{good} the total number of good observations along-scan (*astrometric_n_good_obs_al*) by *Gaia* to compute the astrometric solution; the luminosity L_{\star} ; the negative luminosity uncertainty L_{\star}^{-} ; the positive luminosity uncertainty L_{\star}^{+} ; the GDR3 parallax ϖ ; the corrected GDR3 parallax ϖ_{corr} according to Lindegren et al. (2021); the parallax uncertainty σ_{ϖ} ; population membership based on a study of stellar total space velocity according to Chen et al. (2021), halo stars are more metal poor.

Table A.3. Stellar parameters of the Miras inferred from the simulations.

Name	$P_{1.0}$ [days]	$\Delta P_{1.0}$ [%]	$P_{1.5}$ [days]	$\Delta P_{1.5}$ [%]	$\log(g_{1.0})$ [cgs]	$\log(g_{1.5})$ [cgs]	$R_{1.0}$ [R_{\odot}]	$R_{1.5}$ [R_{\odot}]	$T_{1.0}$ [K]	$T_{1.5}$ [K]
Y And	270	22	254	15	-0.35	-0.27	246	274	3012	3042
RT Aql	380	16	367	12	-0.52	-0.47	302	348	2843	2860
SY Aql	353	1	339	5	-0.48	-0.43	289	330	2879	2898
V335 Aql	225	28	209	19	-0.25	-0.16	221	242	3106	3144
T Aqr	213	5	197	2	-0.22	-0.13	214	232	3136	3177
U Ari	402	8	390	5	-0.55	-0.50	312	362	2816	2830
RU Aur	443	6	434	8	-0.60	-0.56	331	387	2770	2780
R Boo	261	17	245	10	-0.33	-0.25	241	268	3029	3061
T Cap	337	25	323	19	-0.46	-0.40	281	320	2901	2922
CM Car	246	28	230	32	-0.30	-0.21	233	257	3060	3095
U Cet	298	27	283	21	-0.40	-0.33	261	293	2962	2989
R Cha	270	20	254	25	-0.35	-0.27	246	274	3012	3042
S CMi	371	11	358	7	-0.51	-0.46	298	342	2854	2872
U CMi	283	31	267	35	-0.37	-0.29	253	283	2988	3017
W Cnc	464	18	456	16	-0.63	-0.59	340	400	2748	2757
R Col	231	30	215	35	-0.27	-0.17	224	246	3093	3130
T Col	207	9	191	16	-0.21	-0.11	210	228	3151	3194
RY CrA	262	27	247	20	-0.33	-0.25	242	269	3026	3058
X CrB	215	11	199	17	-0.23	-0.13	215	234	3130	3171
R Del	277	3	261	9	-0.36	-0.28	250	279	2999	3028
W Dra	184	36	169	42	-0.15	-0.04	196	210	3212	3260
T Eri	281	11	265	5	-0.37	-0.29	252	282	2992	3021
U Eri	239	13	223	19	-0.28	-0.19	229	252	3075	3111
V Gem	402	46	391	42	-0.55	-0.5	312	362	2815	2829
S Her	261	14	245	19	-0.33	-0.25	242	268	3028	3061
SV Her	215	10	199	16	-0.23	-0.13	215	234	3130	3170
T Her	206	26	190	16	-0.21	-0.11	210	227	3153	3195
T Hor	227	4	211	4	-0.26	-0.16	222	243	3102	3140
RR Hya	290	15	274	20	-0.38	-0.31	257	288	2976	3004
RU Hya	332	1	317	5	-0.45	-0.39	279	316	2908	2930
S Lac	242	1	226	6	-0.29	-0.20	231	254	3067	3103
RR Lib	302	9	287	3	-0.4	-0.33	263	296	2956	2982
R LMi	482	29	475	27	-0.65	-0.61	348	411	2730	2737
RT Lyn	258	34	243	38	-0.32	-0.24	240	266	3034	3067
U Oct	240	21	224	26	-0.29	-0.20	230	253	3072	3108
R Oph	393	30	381	26	-0.54	-0.49	308	356	2827	2842
RY Oph	252	67	236	57	-0.31	-0.23	236	261	3047	3081
SY Pav	219	15	203	6	-0.24	-0.14	217	237	3121	3161
R Peg	421	11	410	9	-0.58	-0.53	321	373	2794	2806
S Peg	331	5	316	1	-0.45	-0.39	278	316	2910	2932
X Peg	209	4	194	4	-0.22	-0.12	212	230	3144	3186
Z Peg	264	19	248	24	-0.33	-0.25	243	270	3023	3055
RZ Sco	274	72	258	62	-0.35	-0.28	249	277	3004	3034
R Sgr	326	21	311	16	-0.44	-0.38	275	312	2918	2941
RV Sgr	286	10	270	15	-0.38	-0.30	255	285	2983	3012
BH Tel	264	22	248	14	-0.33	-0.25	243	270	3024	3056
T Tuc	219	11	203	18	-0.24	-0.14	218	237	3120	3159
T UMa	279	9	263	3	-0.36	-0.29	251	280	2996	3025
RR UMa	209	10	193	16	-0.21	-0.12	212	230	3145	3186
T UMi	236	1	220	6	-0.28	-0.19	227	250	3081	3118
CI Vel	173	25	158	14	-0.12	0.00	189	201	3247	3297
R Vir	236	62	220	51	-0.28	-0.19	227	250	3081	3118
R Vul	226	66	211	54	-0.26	-0.16	222	243	3103	3141

Notes: The subscripts 1.0 denotes quantities derived from the $1.0 M_{\odot}$ simulations, and 1.5 those from the $1.5 M_{\odot}$ simulations. The columns are: Miras' name; the pulsation periods $P_{1.0}$ and $P_{1.5}$ in days; the relative difference between the observed pulsation period and our results $\Delta P_{1.0}$ and $\Delta P_{1.5}$ in %; the effective surface gravity $\log(g_{1.0})$ and $\log(g_{1.5})$, with g in cgs; $R_{1.0}$ and $R_{1.5}$ the radius in R_{\odot} ; $T_{1.0}$ and $T_{1.5}$ the effective temperature in K .

Appendix C: M dwarfs versus AGB stars parallax uncertainty

Our key assumption is that the parallax uncertainty budget in the Mira sample is dominated by the photocentre shift due to the huge AGB convection cells. To test this assumption, one would need a comparison sample of stars with similar properties such as apparent G magnitude, distance, $G_{BP} - G_{RP}$ colour, etc., but ideally without surface brightness inhomogeneities. M-type dwarfs could be useful for a comparison because they have similar $G_{BP} - G_{RP}$ colour as our Miras. Therefore, we searched the SIMBAD database for M5 dwarfs with $G < 15$ mag, which yielded a sample of 240 objects. The list was cross-matched with the *Gaia* DR3 catalogue. Obvious misidentifications between SIMBAD and *Gaia* with $G > 15$ were culled from the list. A Hertzsprung-Russell diagram based on M_G vs. $G_{BP} - G_{RP}$ revealed that the sample still contained several misclassified M-type giant stars. Removing them retained a sample of 99 dwarf stars that have comparable $G_{BP} - G_{RP}$ colour to the Miras sample. However, as M dwarfs are intrinsically much fainter than Miras, the dwarf stars are much closer to the sun than the Miras: their distances vary between ~ 7 and 160 pc, whereas our Mira sample stars are located between 300 and over 5000 pc from the sun. Furthermore, we noticed that a significant fraction of the dwarfs have surprisingly large parallax uncertainties. These could be related to strong magnetic fields on the surfaces of these dwarfs that are the cause of bright flares or large, dark spots, creating surface brightness variations similar to those expected in the AGB stars. A detailed investigations into the reasons for their large parallax uncertainties is beyond the scope of this paper. We therefore decided to not do the comparison with the M dwarfs.

Luckily, the contaminant, misclassified (normal) M giants in the Simbad search appear to be a much better comparison sample. They have overlap with the Mira stars in G magnitude and are at fairly similar distances, between ~ 260 and 1700 pc. The only drawbacks are that the normal M giants are somewhat bluer in $G_{BP} - G_{RP}$ colour than the Miras, and we found only ten suitable M giants in our limited search. Fig. C1 illustrates the location of the M giants together with the Mira sample and the M dwarfs in an HR diagram.

Importantly, we note that the parallax uncertainties of the M giants are all smaller than those of the Miras. This is shown in Fig. C2, where the logarithmic value of the parallax uncertainty is plotted as a function of the logarithm of the distance (here simply taken as the inverse of the parallax). On average, the M giants have parallax uncertainties that are smaller by a factor of 3.5 than those of the Miras. As the M giants are more compact than the Miras and have smaller pressure scale heights, it is plausible that the larger parallax uncertainties of the Miras indeed result from their surface convection cells. We therefore conclude that our key assumption is correct.

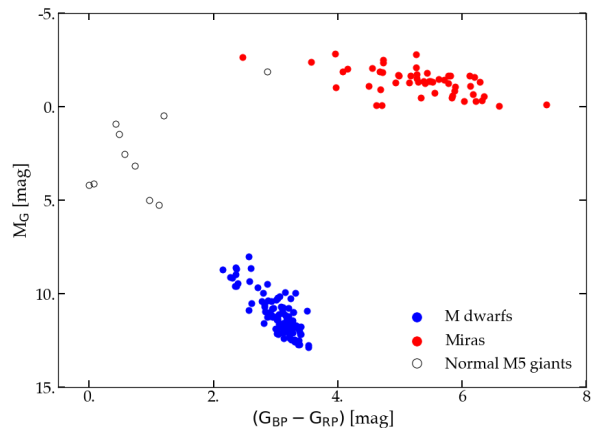


Fig. C1. Hertzsprung-Russell diagram: absolute G magnitude M_G versus $G_{BP} - G_{RP}$ colour from *Gaia* data. In red are the Mira stars of our sample, in blue the M5 dwarfs, and in white the misclassified (normal) M giants.

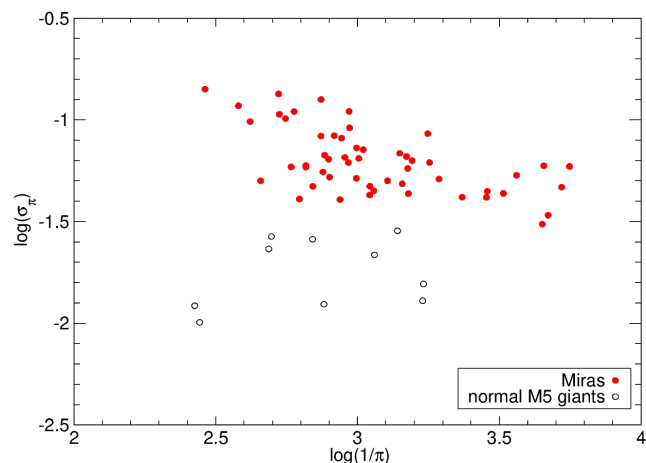


Fig. C2. Log-log of the parallax uncertainty, σ_π , versus the distance, simply taken as the inverse of the parallax, π . We see that the M giants parallax uncertainties are smaller than those of the Miras by a factor of ~ 3.5 .